

Comparison study of counting and fitting methods in search for neutrinoless double beta decays*

Hao-Yang Fu,^{1,2} Wen-Tai Luo,^{1,2,†} Xiang-Pan Ji,³ and Shao-Min Chen^{1,2,4}

¹Department of Engineering Physics, Tsinghua University, Beijing, China

²Center for High Energy Physics, Tsinghua University, Beijing, China

³School of Physics, Nankai University, Tianjin, China

⁴Key Laboratory of Particle & Radiation Imaging, Tsinghua University, Ministry of Education, Beijing, China

In the search for neutrinoless double beta decay ($0\nu\beta\beta$) experiments, common methods for sensitivity calculations include the counting method and the spectrum fitting method. This research compares their difference in sensitivity under various energy resolutions. Additionally, the performance of high and low Q -value $0\nu\beta\beta$ isotopes is compared. The results of this research could provide guidance on the choice of methods for sensitivity calculations, energy resolution and $0\nu\beta\beta$ isotopes for future $0\nu\beta\beta$ experiments.

Keywords: Neutrinos, Neutrinoless double-beta decay, MC simulation, Analysis and statistical methods

I. INTRODUCTION

Neutrinoless double beta decay ($0\nu\beta\beta$), $(A, Z) \rightarrow (A, Z + 2) + 2e^-$, is an extremely rare decay process that occurs in certain nuclides [1]. The investigation of $0\nu\beta\beta$ plays a significant role in exploring physics beyond the standard model [2]. The half-life of $0\nu\beta\beta$ could also provide crucial information for determining the neutrino mass hierarchy, since the effective mass of Majorana neutrinos $\langle m_{\beta\beta} \rangle$ is highly related to the half-life. The existence of $0\nu\beta\beta$ decay would demonstrate that neutrinos are Majorana fermions.

Currently, there is no confirmed experimental evidence for neutrinoless double beta decay. Extensive experimental efforts are being dedicated to the search for $0\nu\beta\beta$ [3–13]. These experimental studies typically employ two methods to estimate the sensitivity to the half-life of $0\nu\beta\beta$. One is the counting method, which involves statistical analysis of events within a selected region of interest (ROI). The counting method relies on the number of events in the ROI. The other is the fitting method, which utilizes spectrum fitting to calculate the sensitivity. Despite the fact that the fitting method requires a detailed study of the background, it is capable of utilizing information from events outside the ROI. This research examined the differences in sensitivity between the two methods.

Currently, the best results in $0\nu\beta\beta$ experiments have come from the KamLAND-Zen experiment using a liquid scintillator detector [12], which has the advantage of high exposure to $0\nu\beta\beta$ nuclei. In this study, we chose to simulate a liquid scintillator detector as an example for our study. The detector simulations were performed with an energy resolution δ (defined by the standard deviation σ_E at 1 MeV as $\delta = \frac{\sigma_E}{1\text{MeV}}$) ranging from 1% to 7%. This made the conclusion of this research applicable to other detector types in this energy resolution range, such as time projection chamber (TPC) detectors.

Furthermore, the studied isotopes in this research were selected as ^{150}Nd and ^{130}Te . These isotopes represent the high Q -value (approximately 3.37 MeV) and low Q -value

(approximately 2.53 MeV) isotopes. The purpose of this research is to provide guidance for future experiments using various isotopes in the selection of appropriate methods for sensitivity calculations.

Section II describes the simulation setup. Section III presents the background of this research. Section IV provides a detailed description of the counting and fitting methods, together with a comparison of their results. Section V presents a discussion, and Section VI concludes.

II. DETECTOR SETUP AND SIMULATION

A. Detector setup

The geometry of the liquid scintillator detector used in this research is similar to JUNO [14]. The general structure of the multi-hundred-ton detector is shown in Fig. 1. The main body of the detector is a 500-ton liquid scintillator enclosed in a 5-meter-radius acrylic sphere. The acrylic sphere is wrapped around by the mineral oil. There is a stainless steel support frame for the photomultiplier tubes (PMT) at a radius of 6 meters. Thousands of 8-inch PMTs are placed on the support frame. The outer layer is a cubic water tank with a side length of 12 meters.

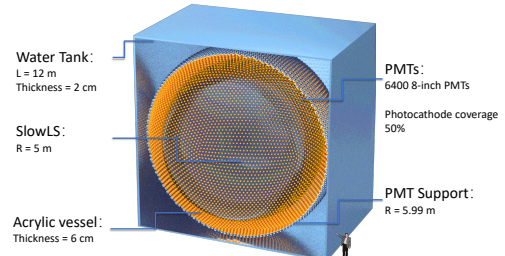


Fig. 1. A simple concept graphic of the detector geometry used in simulations.

In this research, the liquid scintillator is loaded with $0\nu\beta\beta$ isotopes by a specific mass fraction. This fraction is set to be 1% for natural Nd and Te [15–17], which corresponds to a mass of 0.285 ton for ^{150}Nd and 1.71 ton for ^{130}Te .

* Supported by the National Natural Science Foundation of China (12127808).

† Corresponding author, luowt@mail.tsinghua.edu.cn

62

B. Simulation

63 The detector simulations used a simulation package named
 64 Jinping Simulation and Analysis Package (JSAP). The JSAP
 65 is based on GEANT4 and has some features, which include
 66 the generator, detector simulation, dark noise and pre-trigger,
 67 waveform generation, and trigger. The details of JSAP were
 68 described in [18].

69

III. NEUTRINOLESS DOUBLE BETA DECAY EXPERIMENT BACKGROUNDS

70

71 The $0\nu\beta\beta$ experiment backgrounds have various sources,
 72 including two-neutrino double beta decay ($2\nu\beta\beta$), solar neu-
 73 trinos, radioactive and cosmogenic backgrounds. These back-
 74 grounds will mask the $0\nu\beta\beta$ signals. The simulations in this
 75 research are based on the China Jinping Underground Lab-
 76 oratory (CJPL). At the CJPL, the cosmic ray flux and the
 77 cosmogenic background are one-thousandth of those in the
 78 KamLAND-Zen experiment [19, 20], causing them to be neg-
 79 ligible. In this research, only the $2\nu\beta\beta$, solar neutrino, and
 80 radioactive backgrounds are considered.

81

A. Two-neutrino double beta decay background

82 The $2\nu\beta\beta$ is an intrinsic background in $0\nu\beta\beta$ experiments.
 83 Similar to the $0\nu\beta\beta$ reaction, the $2\nu\beta\beta$ reaction, $(A, Z) \rightarrow$
 84 $(A, Z + 2) + 2e^- + 2\bar{\nu}_e$, generates a background through
 85 the energy deposition of the two electrons in the final state.
 86 Since the anti-electron neutrinos in the final state can take
 87 away energy, the total kinetic energy of two electrons forms
 88 a continuous spectrum, with its endpoint being the reaction's
 89 Q -value. This energy spectrum can be approximately given
 90 by [21]

$$\frac{dN}{dK} \approx (K - Q)^5 \left(1 + 2K + \frac{4}{3}K^2 + \frac{1}{3}K^3 + \frac{1}{30}K^4 \right), \quad (1)$$

91 where K is the total kinetic energy of the two final state elec-
 92 trons and Q is the reaction's Q -value. This equation neglects
 93 the effect of double Fermi transitions and uses the Interac-
 94 tion Boson Model with the closed approximation, while the
 95 Fermi factor is computed using the Primakoff-Rosen approx-
 96 imation [22].

97 Fig. 2 shows the $2\nu\beta\beta$ and $0\nu\beta\beta$ two-electron total kinetic
 98 energy spectra with an energy resolution of $3\%/\sqrt{E(\text{MeV})}$
 99 for ^{150}Nd . The ratio of the half-life of $2\nu\beta\beta$ to the half-life of
 100 $0\nu\beta\beta$ is set to be $1:10^6$, since the ratio of the half-life of $2\nu\beta\beta$
 101 to the lower limit of the half-life of $0\nu\beta\beta$ in the KamLAND-
 102 Zen experiment is approximately $1:10^5$ [11].

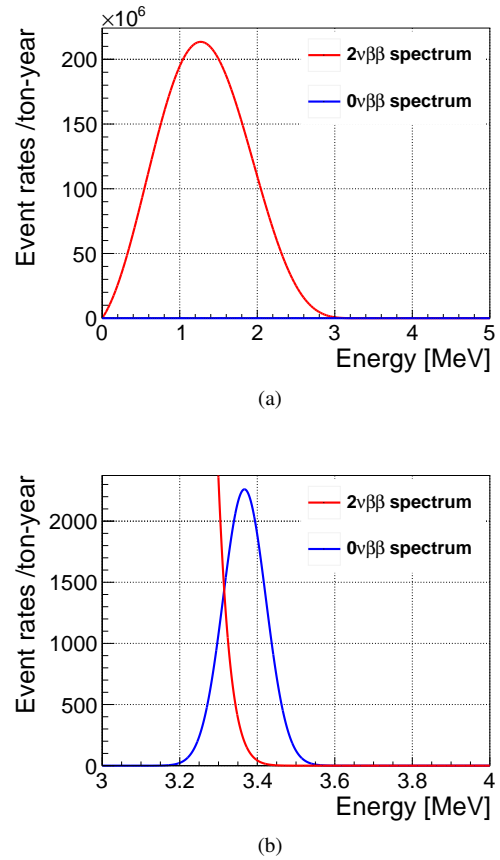


Fig. 2. The full view (a) and the enlarged view (b) of two-electron total kinetic energy spectra of $2\nu\beta\beta$ and $0\nu\beta\beta$, obtained with an energy resolution of $3\%/\sqrt{E(\text{MeV})}$. The ratio of the half-life of $2\nu\beta\beta$ to the half-life of $0\nu\beta\beta$ is set to be $1:10^6$.

B. Solar neutrino background

104 Solar neutrinos are produced through nuclear fusion pro-
 105 cesses occurring in the core of the Sun. For most nuclides
 106 of interest in the $0\nu\beta\beta$ experiments, the Q -value falls within
 107 the region of $>2.4 \text{ MeV}$ [2]. Within this energy range, only
 108 the ^8B and the hep neutrinos exhibit significant contribu-
 109 tions [23]. Since the ^8B component is approximately hun-
 110 dreds of times higher than the hep component, the contribu-
 111 tion of the hep component of solar neutrinos is ignored in this
 112 research.

114 1. Neutrino-electron elastic scattering

115 The primary mechanism by which solar neutrinos con-
 116 tribute to the background in the $0\nu\beta\beta$ experiments is through
 117 elastic scattering (ES). Theoretical studies can provide the
 118 survival probabilities of solar neutrinos reaching Earth [24].
 119 The flux of solar neutrinos $\frac{d\phi_i(E_\nu)}{dE_\nu}$, where $i = e, \mu, \tau$, can be
 120 calculated using these survival probabilities. By combining
 121 this flux with the neutrino-electron elastic scattering cross-

122 sections $\frac{d\sigma_i(E_e, E_\nu)}{dE_e}$ [25], the recoil electron spectrum can be
123 derived as

$$\frac{dN_e(E_e)}{dE_e} = N_0 \times t \times \sum_i^{\text{flavours}} \int dE_\nu \frac{d\phi_i(E_\nu)}{dE_\nu} \frac{d\sigma_i(E_e, E_\nu)}{dE_e}, \quad (2)$$

124 where N_0 is the number of electrons in the target and t is the
125 measuring time.

126 As a result, the ^8B recoil electron spectrum with
127 $3\%/\sqrt{E(\text{MeV})}$ energy resolution is shown in Fig. 3.

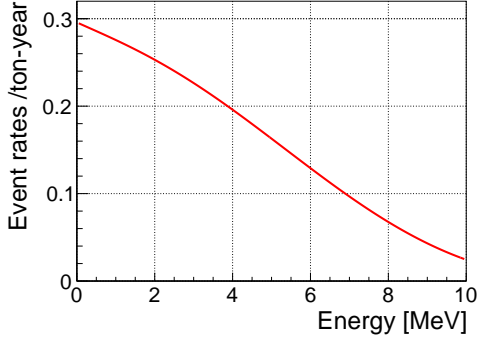


Fig. 3. The neutrino-electron elastic scattering electron recoil spectrum of ^8B neutrinos, obtained with an energy resolution of $3\%/\sqrt{E(\text{MeV})}$.

2. Decay nuclide capture background

130 Neutrinos can be captured by nuclides in the detector
131 through a charged current (CC) process. Ref. [26, 27] indi-
132 cates that the $0\nu\beta\beta$ nuclide would capture neutrinos and then
133 undergo the single β decay (SB) to release an electron (and
134 possibly photons):

$$\begin{aligned} \text{CC} : (A, Z-1) + \nu &\rightarrow (A, Z) + e^- + \gamma(s) + Q_\nu, \\ \text{SB} : (A, Z) &\rightarrow (A, Z+1) + e^- + \gamma(s) + Q_\beta. \end{aligned} \quad (3)$$

136 This research follows the calculations from [26, 27] to ob-
137 tain the energy spectrum of β or $\beta + \gamma$. For example, ^{150}Nd
138 undergoes the CC process to become ^{150}Pm . Subsequently,
139 ^{150}Pm undergoes the SB process to the ground state or ex-
140 cited states of ^{150}Sm . This process would emit an electron
141 and probably de-excitation photons. The calculation consid-
142 ers all decay paths of ^{150}Pm with a branching ratio greater
143 than 1% and sets the lower limit of the branching ratio for
144 the ground state at 10%. This calculation results in a total
145 branching ratio of 99.7%. The energy spectrum of β decay
146 used here is approximately given by [28]

$$\frac{dN}{dE} \approx (E_0 - E_e)^2 E_e p_e F(Z, E_e), \quad (4)$$

148 where E_0 is the energy of the β decay endpoint, E_e and p_e
149 are the energy and momentum of the final state electron, and
150 $F(Z, E_e)$ is the Fermi function.

151 ^{130}Te follows a similar process, undergoing the CC process
152 to transform into ^{130}I , which subsequently undergoes the SB
153 process to convert into ^{130}Xe . Fig. 4 provides the total energy
154 spectra of the capture of neutrinos by ^{150}Nd and ^{130}Te , with
155 an energy resolution of $3\%/\sqrt{E(\text{MeV})}$.

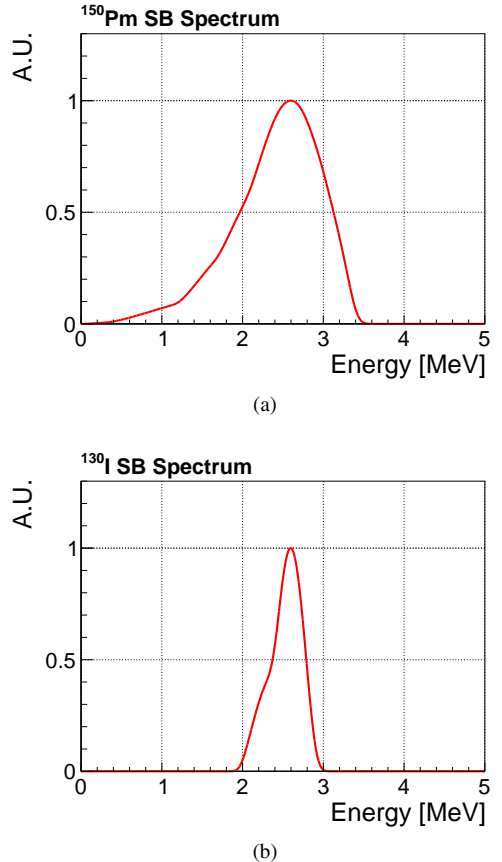


Fig. 4. The single beta (SB) energy spectra of (a) ^{150}Pm and (b) ^{130}I process, which come from the charged current process of ^{150}Nd and ^{130}Te . The spectra are drawn with an energy resolution of $3\%/\sqrt{E(\text{MeV})}$.

C. Radioactive background

157 Radioactive isotopes in materials emit α , β and γ particles.
158 These particles can deposit energy in the detector, contribut-
159 ing to the radioactive background. The primary isotopes that
160 contribute to this background are those of the decay chains
161 from ^{238}U and ^{232}Th , along with the ^{40}K isotopes. The high
162 energy γ from these sources, such as the 2.61 MeV γ of ^{208}Tl ,
163 are capable of penetrating the detector materials and entering
164 the detector center, depositing the energy to form background
165 events. Table 1 shows the radioactive purity for various ma-
166 terials in the simulation.

Table 1. The radioactive purity of different detector materials used in the simulation.

Materials	^{238}U [g/g]	^{232}Th [g/g]	^{40}K [g/g]
Liquid scintillator[29]	1×10^{-16}	1×10^{-16}	1×10^{-18}
Acrylic[30]	6×10^{-13}	1.6×10^{-12}	null
Stainless steel [31]	3.7×10^{-10}	2.8×10^{-9}	4.5×10^{-7}
Water [29]	1×10^{-13}	2×10^{-13}	2×10^{-14}
PMT glass [29]	3×10^{-8}	1×10^{-8}	2×10^{-9}

167

D. Simulation for backgrounds

204

168 This research used the Monte Carlo (MC) method to simu-
169 late the $0\nu\beta\beta$ signals and $2\nu\beta\beta$, solar neutrino, and radioac-
170 tive backgrounds. This method involves random sampling
171 from the energy spectrum of each background to generate
172 background events. The effect of energy resolution δ (ranging
173 from $1\%/\sqrt{E(\text{MeV})}$ to $7\%/\sqrt{E(\text{MeV})}$) on the shape of the
174 energy spectra is incorporated by convolving with a Gaussian
175 function $N\left(\mu = 0, \sigma = \frac{\delta}{\sqrt{E(\text{MeV})}}\right)$.

176 For radioactive backgrounds, it is necessary to first ob-
177 tain their visible energy (electron equivalent energy, unit is
178 MeVee) spectra. To obtain these visible energy spectra, a de-
179 tector simulation was conducted. In this detector simulation,
180 for the isotope decay that occurs in the liquid scintillator, the
181 ^{238}U decay chain, the ^{232}Th decay chain and ^{40}K were con-
182 sidered. For isotope decay that occurs outside the liquid scin-
183 tillator, only specific nuclei were considered. These nuclei in-
184 cluded ^{210}Tl , ^{214}Bi and ^{234}Pa in the ^{238}U decay chain, ^{208}Tl ,
185 ^{212}Bi and ^{228}Ac in the ^{232}Th decay chain and ^{40}K . The nuclei
186 that would undergo α decay were not considered since the α
187 particles would quench in the liquid scintillator and have low
188 visible energy (<1.5 MeVee). Furthermore, nuclei with vis-
189 ible energies lower than 1.5 MeVee were not considered ei-
190 ther, since they fall outside the fitting range (1.5~4.8 MeV).
191 With the spectra of radioactive backgrounds, it is capable
192 of performing MC simulations. As a sample, Fig. 5 shows
193 the radioactive background energy spectra in the liquid scin-
194 tillator (5-meter-radius sphere) with an energy resolution of
195 $3\%/\sqrt{E(\text{MeV})}$.

196 As a result, Fig. 6 shows a sample of simulated background
197 spectra of 1% natural Nd-loaded with an energy resolution of
198 $3\%/\sqrt{E(\text{MeV})}$.

IV. COUNTING AND FITTING METHODS

200 The mathematical principles of the counting and fitting
201 methods are described here, together with the fiducial vol-
202 umes defined for both methods and the ROI selection of the
203 counting method.

A. Counting method

205 The mathematical principles of the counting method are
206 described in Section IV A 1. The fiducial volume and ROI
207 selection for the counting method are described in Sec-
208 tion IV A 2.

1. Mathematical principles of counting method

209 Based on the total number of events N_{ROI} observed in the
210 ROI, the upper limit S_{limit} for the signal count at a given con-
211 fidence level (C.L.) can be defined as

$$213 \quad P(S_{\text{limit}} > S) \geq 1 - \alpha, \quad (5)$$

214 where the $1 - \alpha$ is the value of the confidence level.

215 For experiments with a large number of background events
216 in the ROI, the Poisson distribution of N_{ROI} (i.e., $\pi(\lambda =$
217 $B+S)$) can be approximated as a normal distribution: $N(\mu =$
218 $B+S, \sigma^2 = B+S)$, where B and S are the expected numbers
219 of background and signal in the ROI, respectively. Assuming
220 the value of B is known in the experiment, the one-sided con-
221 fidence interval for the estimate of the signal number \hat{S} can
222 be obtained as [32]:

$$223 \quad S_{\text{limit}} = N_{\text{ROI}} - B + n_{\sigma} \sqrt{N_{\text{ROI}}}, \quad (6)$$

224 where n_{σ} is corresponding to the confidence level. For ex-
225 ample, a 90% confidence level ($\alpha = 0.1$) corresponds to a
226 $n_{\sigma} = 1.28$.

227 With the number of signals much lower than the back-
228 grounds, the equation (6) can be further approximated as:

$$229 \quad S_{\text{limit}} = n_{\sigma} \sqrt{N_{\text{ROI}}}. \quad (7)$$

230 For a specific $0\nu\beta\beta$ isotope, the upper limit S_{limit} can be con-
231 verted into the lower limit of the $0\nu\beta\beta$ half-life as following:

$$232 \quad T_{1/2}^{\text{limit}} = \frac{N_A \times \ln 2}{n_{\sigma} \sqrt{N_{\text{ROI}}}} \frac{M_{\text{iso}} \times 10^6}{A_{\text{iso}}} \times t \times \epsilon, \quad (8)$$

233 where N_A is Avogadro's number, M_{iso} is the total mass of
234 the $0\nu\beta\beta$ reaction isotope in the detector (in ton) and times
235 the 10^6 to transfer into gram, A_{iso} is the atomic number of
236 the isotope, t is the detector run time and ϵ is the detection
237 efficiency.

238 By substituting $\Delta E \times b$ for N_{ROI} in (8), we have

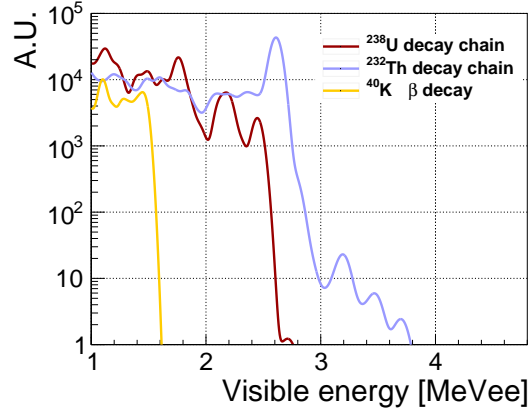


Fig. 5. Visible energy spectra of the radioactive backgrounds in liquid scintillator (5-meter-radius sphere) under a $3\%/\sqrt{E(\text{MeV})}$ energy resolution. For radioactive backgrounds in the liquid scintillator, the ^{238}U decay chain, the ^{232}Th decay chain and ^{40}K are considered. When outside the liquid scintillator, only a subset of nuclei are simulated, including ^{228}Ac , ^{212}Bi , ^{214}Bi , ^{234}Pa , ^{208}Tl , ^{210}Tl and ^{40}K .

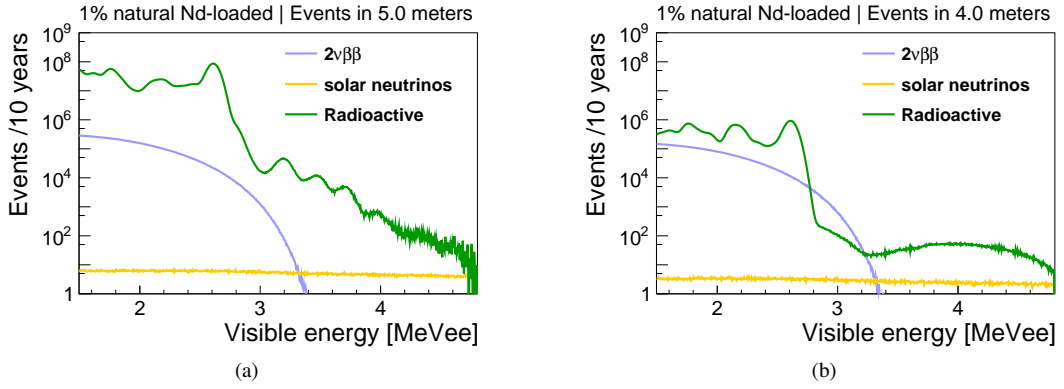


Fig. 6. A sample of simulated background spectra of 1% natural Nd-loaded within the (a) 5-meters-radius sphere and the (b) 4-meters-radius sphere. The energy resolution is set to $3\%/\sqrt{E(\text{MeV})}$.

$$T_{1/2}^{\text{limit}} = \frac{N_A \times \ln 2}{n_\sigma \sqrt{\Delta E} \times b} \frac{M_{\text{iso}} \times 10^6}{A_{\text{iso}}} \times t \times \epsilon, \quad (9)$$

where ΔE is the width of ROI and b is background count per energy unit. This equation can be used to estimate the sensitivity for an experiment [32].

2. Fiducial volume and ROI searching

Selecting the appropriate fiducial volume and the ROI range can enhance the sensitivity of the counting method. To determine the suitable fiducial volume and ROI, different values of them were tested, as described in detail below.

The radius was varied to optimize the fiducial volume with forty values ranging from 1.1 to 5.0 meters, with a step size of 0.1 meters. Additionally, as the fiducial volume reduced, an exponential decrease in the radioactive background originating from outside the liquid scintillator was observed. This reduction arises because the liquid scintillator outside the fiducial volume acts as a buffer layer. This reduction also leads

to changes in the shape of the spectrum for different fiducial volumes, as shown in Fig. 6. Therefore, the spectral shape for each fiducial volume condition was individually studied by simulating the radioactive backgrounds.

The selection of the ROI requires the determination of an appropriate ROI width and the center position of the ROI. To select a suitable ROI width, the ROI width ΔE_R , ranging from 0.02 to 1 MeV, was divided into fifty values with a step size of 0.02 MeV. Regarding the center position, the ROI was set as $[Q - 0.5\Delta E_R, Q + 0.5\Delta E_R]$, $[Q - 0.25\Delta E_R, Q + 0.75\Delta E_R]$ and $[Q, Q + \Delta E_R]$, since the $2\nu\beta\beta$ backgrounds are not symmetric near the Q -value.

The most suitable condition for the counting method was searched with an MC data set, and Fig. 7 shows the samples of the searching process. Then, for specific energy resolutions and isotopes, the fiducial volume radius and ROI corresponding to the highest 90% C.L. sensitivity were chosen. The fiducial volume and ROI selection results for the counting method are shown in Table 2.

As a result, the fiducial volume of ^{130}Te is smaller than that

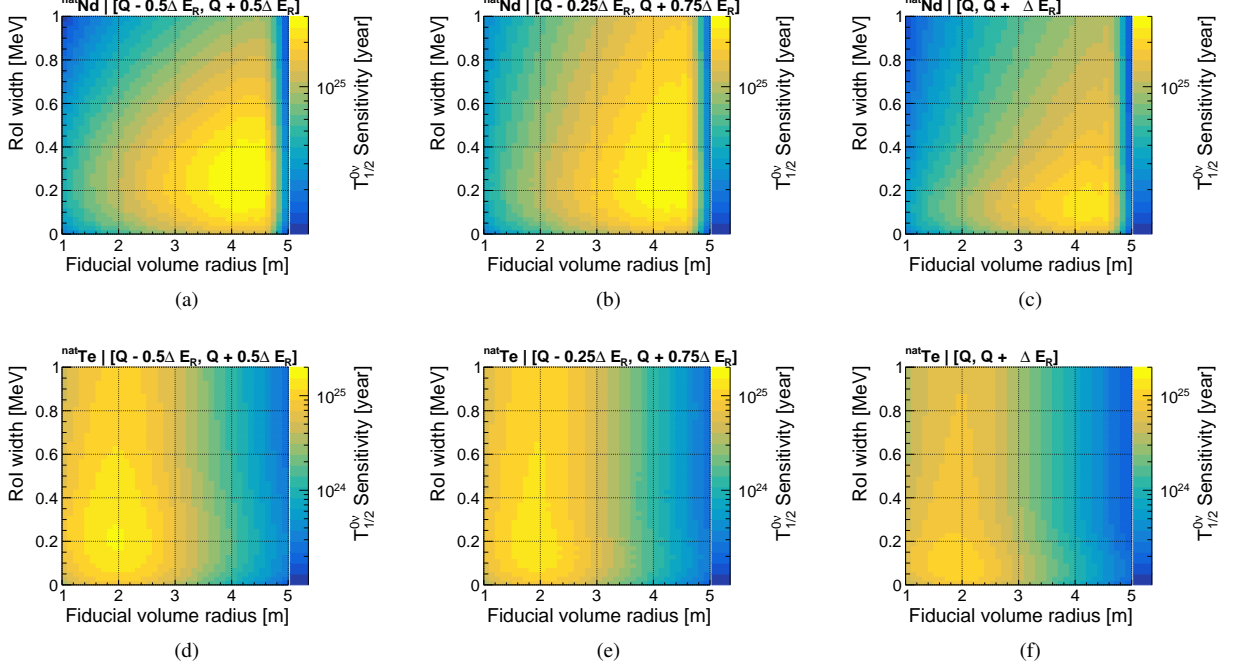


Fig. 7. The 90% C.L. sensitivities of $0\nu\beta\beta$ half-life vs. ROI width ΔE_R and fiducial volume radius, derived with 1% natural Nd-loaded (a,b,c) and 1% natural Te-loaded (d,e,f) under an energy resolution of $3\%/\sqrt{E}(\text{MeV})$ and a run time of 10 years (corresponding to the total exposure 2.85 ton-year for ^{150}Nd and 17.10 ton-year for ^{130}Te). The ROIs are set as $[Q - 0.5\Delta E_R, Q + 0.5\Delta E_R]$ for (a,d), $[Q - 0.25\Delta E_R, Q + 0.75\Delta E_R]$ for (b,e) and $[Q, Q + \Delta E_R]$ for (c,f).

Table 2. The fiducial volume and ROI selection for counting method with ^{150}Nd and ^{130}Te . The second column is the energy resolution δ , the third column is the radius of the fiducial volume, the fourth column is the ROI range and the fifth column is the exposure of the isotopes with the 1% natural Nd-loaded and 1% natural Te-loaded. The fiducial volume of ^{130}Te is smaller than that of ^{150}Nd because the radioactive backgrounds near the Q -value of ^{130}Te are much higher, so a smaller fiducial volume is needed to exclude these backgrounds.

Isotope	Energy resolution δ	Fiducial volume radius [m]	ROI range [MeV]	Exposure [ton-year]
^{150}Nd	0.01	4.6	$[3.35, 3.43]^2$	2.22
^{150}Nd	0.02	4.2	$[3.28, 3.45]^1$	1.69
^{150}Nd	0.03	4.3	$[3.25, 3.49]^1$	1.81
^{150}Nd	0.04	4.3	$[3.30, 3.59]^2$	1.81
^{150}Nd	0.05	4.6	$[3.27, 3.65]^2$	2.22
^{150}Nd	0.06	4.6	$[3.25, 3.72]^2$	2.22
^{150}Nd	0.07	4.6	$[3.37, 3.82]^3$	2.22
^{130}Te	0.01	2.3	$[2.50, 2.56]^1$	1.66
^{130}Te	0.02	2.2	$[2.46, 2.60]^1$	1.46
^{130}Te	0.03	2.1	$[2.42, 2.64]^1$	1.27
^{130}Te	0.04	2.0	$[2.37, 2.69]^1$	1.09
^{130}Te	0.05	2.0	$[2.31, 2.75]^1$	1.09
^{130}Te	0.06	2.1	$[2.26, 2.80]^1$	1.27
^{130}Te	0.07	2.1	$[2.24, 2.82]^1$	1.27

¹ ROI set as $[Q - 0.5\Delta E_R, Q + 0.5\Delta E_R]$.

² ROI set as $[Q - 0.25\Delta E_R, Q + 0.75\Delta E_R]$.

³ ROI set as $[Q, Q + \Delta E_R]$.

275 of ^{150}Nd because the radioactive backgrounds near the Q -
 276 value of ^{130}Te are much higher, so a smaller fiducial volume
 277 is needed to exclude these backgrounds.

278

B. Fitting method

279 The fitting method requires a detailed study of the back-
 280 ground, and it is able to use events outside of the ROI. This
 281 research uses the Chi-squared (χ^2) fitting method. The form
 282 of the χ^2 function is described in Section IV B 1. The math-
 283 ematical principle of the fitting method is described in Sec-
 284 tion IV B 2.

285

1. Chi-squared function

286 The fitting method used in this research utilizes a binned
 287 χ^2 fitting. The test statistic χ^2 consists of two components as

288

$$\chi^2 = \chi^2_{\text{energy}} + \chi^2_{\text{penalty}}, \quad (10)$$

289 where

290

$$\chi^2_{\text{energy}} = 2 \sum_{i=1}^{N_{\text{bin}}} \left(n_i \log \frac{n_i}{v_i} + v_i - n_i \right), \quad (11)$$

291 is a Poisson format χ^2 [33] and

292

$$\chi^2_{\text{penalty}} = \sum_{k=1}^{N_{\text{bkg}}} \left(\frac{v_k^{\text{bkg}} - n_k^{\text{bkg}}}{\sigma_k^{\text{bkg}}} \right)^2, \quad (12)$$

293 where, N_{bin} denotes the number of bins in the fitting range,
 294 n_i is the observed number of events in the i -th bin, and
 295 $v_i = v_i^{\text{signal}} + \sum_k v_{ki}^{\text{bkg}}$ is the expected number of events in
 296 the i -th bin, k represents for the k -th background. N_{bkg} de-
 297 notes the number of background types, $v_k^{\text{bkg}} = \sum_i v_{ki}^{\text{bkg}}$
 298 represents the expected number of events of the k -th back-
 299 ground, n_k^{bkg} represents its measured value and σ_k^{bkg} is the
 300 standard deviation of the measured value.

301 This research utilizes the TMINUIT class from the CERN
 302 ROOT [34] software package and employs its default opti-
 303 mization algorithm MIGRAD to minimize the χ^2 function.
 304 Fig. 8 shows a sample of χ^2 fitting with an energy resolution
 305 of $3\%/\sqrt{E(\text{MeV})}$ and a detector run time of 10 years (cor-
 306 sponding to the exposure of 1.35 ton-year for ^{150}Nd and 1.46
 307 ton-year for ^{130}Te).

309

2. Mathematical principles of fitting method

310 The fitting method in this research used a binned χ^2 fit-
 311 ting method, and the Feldman-Cousins method [35] (FC
 312 method) is used to calculate confidence intervals. For a multi-
 313 dimensional sample, constructing a confidence band requires

314 computationally intensive calculations and is difficult to vi-
 315 sualize. Therefore, a toy MC method named profiled FC
 316 method [36] was performed to solve this problem, which will
 317 be briefly introduced in the following.

318 For a specific value of the parameter $\mu = \mu_s$, multiple toy
 319 MC samples x_i will be generated, each corresponding to a
 320 $\Delta\chi_j^2(x_i; \mu_s) = \chi^2(x_i; \mu_s) - \chi^2(x_i; \mu_{\text{best}})$, where μ_{best} is
 321 the best fitting result of the parameter μ . Then, a certain value
 322 of $\Delta\chi_c^2(\mu_s)$ should be derived by making $1 - \alpha$ of toy MC
 323 samples satisfy $\Delta\chi_j^2(x_i; \mu_s) < \Delta\chi_c^2(\mu_s)$. After repeating
 324 this process for enough points of μ_s , one can get a curve of
 325 $\Delta\chi_c^2(\mu_s)$, then the confidence interval of μ for a specific sam-
 326 ple x can be derived as:

$$I_\mu = \{\mu | \Delta\chi^2(x; \mu) < \Delta\chi_c^2(\mu)\}. \quad (13)$$

327 By performing the profiled FC method, one can avoid the
 328 construction of confidence bands in a multidimensional $x - \mu$
 329 space. However, the profiled FC method still has the problem
 330 of choosing the values of the nuisance parameters during the
 331 toy MC generation process. One of the solutions is to pre-
 332 assign the values of the nuisance parameters to generate toy
 333 MC samples using a predetermined nuisance function [37].

334 In this research, the total count of each background $\{N_k\}$
 335 and the $0\nu\beta\beta$ signal N_s were set as the fitting parameters,
 336 while the samples are the events in each bin $\{n_i\}$. The pro-
 337 filed FC method can be used to determine the confidence in-
 338 terval for the signal count N_s using the equation (13). In
 339 most situations, this confidence interval would encompass 0
 340 and become an upper limit $N_{s|\text{upper}}$. This would allow for
 341 a straightforward conversion from an upper limit on the sig-
 342 nal count $N_{s|\text{upper}}$ into a lower limit on the $0\nu\beta\beta$ half-life as
 343 $T_{\text{lower}}^{0\nu} = \frac{N_A \times \ln 2}{N_{s|\text{upper}}} \frac{M_{\text{iso}} \times 10^6}{A_{\text{iso}}} \times t \times \epsilon$, where the definitions of
 344 constants are the same as in equation (8).

345 Furthermore, in this research, this method is used to obtain
 346 the half-life sensitivity of $0\nu\beta\beta$. Sensitivity is obtained by
 347 generating toy MC samples with zero signal, calculating the
 348 $0\nu\beta\beta$ half-life lower limit for each MC sample, and choosing
 349 the median of the results.

3. Fiducial volume cut for fitting method

351 The fiducial volume cut searching for fitting method is
 352 same as the counting method described in Section IV A 2.
 353 Fig. 9 shows a sample of fiducial volume searching for the
 354 fitting method derived with ^{150}Nd and ^{130}Te , under an en-
 355 ergy resolution of $3\%/\sqrt{E(\text{MeV})}$ and detector run time of
 356 10 years, while the exposures of ^{150}Nd and ^{130}Te are change
 357 with the fiducial volume radius. Subsequently, for specific
 358 resolutions and isotopes, the fiducial volume radius corre-
 359 sponding to the highest 90% C.L. sensitivity of the $0\nu\beta\beta$
 360 half-life was chosen. As a result, Table 3 gives the fiducial
 361 volume cuts.

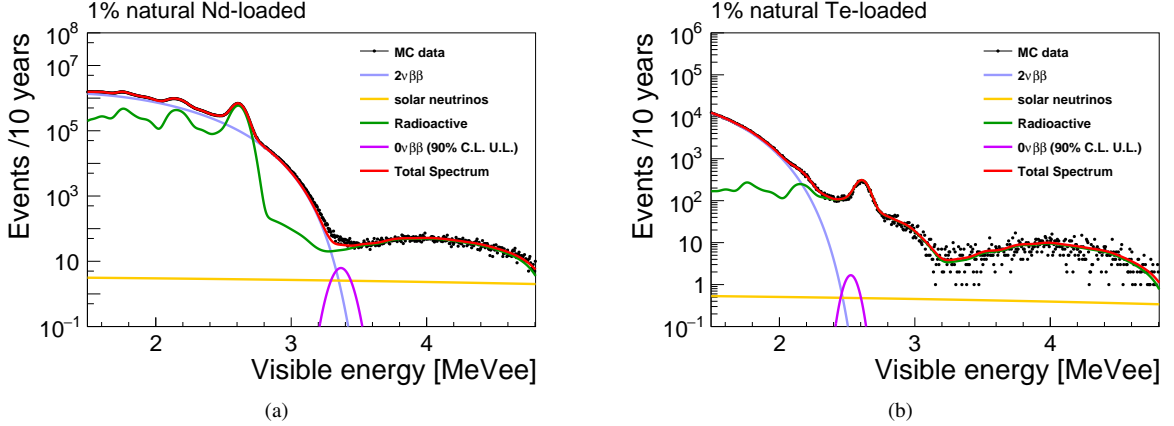


Fig. 8. Energy spectra of simulated events within the fiducial volume drawn together with best-fit backgrounds and the 90% C.L. upper limit for $0\nu\beta\beta$ of (a) 1% natural Nd-loaded in a 3.9-meter-radius sphere and (b) 1% natural Te-loaded in a 2.2-meter-radius sphere. The energy resolution is set to $3\%/\sqrt{E(\text{MeV})}$, detector run time is 10 years (corresponding to the exposure 1.35 ton-year for ^{150}Nd and 1.46 ton-year for ^{130}Te). Lines are fitting results and the black points are MC data.

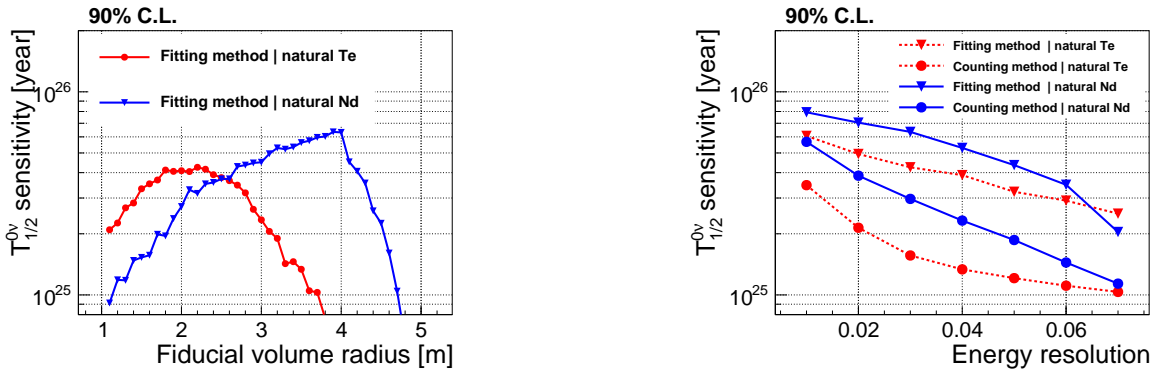


Fig. 9. A sample of fiducial volume search process for fitting method. The 90% C.L. sensitivities are derived with an energy resolution of $3\%/\sqrt{E(\text{MeV})}$ and a detector run time of 10 years. The red line is the result derived with 1% natural Te-loaded and the blue line is the result derived with 1% natural Nd-loaded.

363

C. Comparison of counting and fitting methods

364 The counting and fitting methods are compared by the ob-
 365 tained 90% C.L. sensitivities of the $0\nu\beta\beta$ half-life. The com-
 366 parison was performed with different $0\nu\beta\beta$ isotopes (^{130}Te
 367 and ^{150}Nd) and different energy resolutions, while the other
 368 conditions are shown in Table 2 and Table 3. These half-life
 369 sensitivities were derived with optimal fiducial volume and
 370 ROI, and the results are shown in Fig. 10.

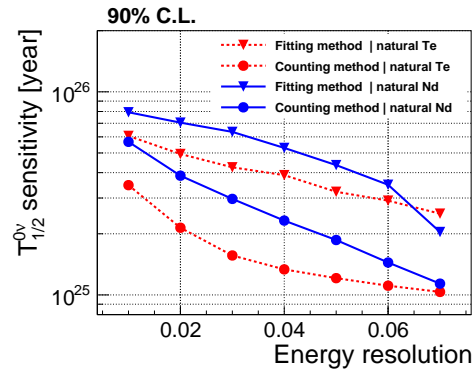


Fig. 10. The 90% C.L. sensitivity of $0\nu\beta\beta$ half-life of ^{130}Te and ^{150}Nd vs. energy resolution for fitting and counting methods. The red dashed lines are derived with 1% natural Te-loaded and the blue solid lines are derived with 1% natural Nd-loaded. Other conditions are shown in Table 2 and Table 3.

371 Under all energy resolution conditions used in this re-
 372 search, the fitting method achieves a higher sensitivity in the
 373 $0\nu\beta\beta$ half-life compared to the counting method.

374 For the fitting method, the sensitivity of the high Q -value
 375 isotope (^{150}Nd) shows a sharp decline when the energy reso-
 376 lution exceeds $6\%/\sqrt{E(\text{MeV})}$, and makes the sensitivity of
 377 the fitting method of ^{150}Nd lower than ^{130}Te at the energy res-
 378 olution of $7\%/\sqrt{E(\text{MeV})}$. These phenomena are discussed
 379 in Section V B.

380 For the counting method, the sensitivity of the high Q -
 381 value isotope (^{150}Nd) decreases faster than that of the low Q -
 382 value isotope (^{130}Te). This is because the main background
 383 for the low Q -value isotope is the radioactivity background,
 384 while for the high Q -value isotope, its main background is
 385 the $2\nu\beta\beta$ background. The $2\nu\beta\beta$ background within the
 386 ROI will increase rapidly as the energy resolution deterio-
 387 rates, leading to a faster decrease in sensitivity of the counting

Table 3. The fiducial volume cuts for fitting method with ^{150}Nd and ^{130}Te . The Second column is the energy resolution δ , the third column is the radius of the sphere corresponding to the fiducial volume bins and the fourth column is the exposure of the isotopes with the 1% natural Nd-loaded and 1% natural Te-loaded.

Isotope	Energy resolution δ	Fiducial volume radius [m]	Exposure [ton-year]
^{150}Nd	0.01	4.0	1.46
^{150}Nd	0.02	4.0	1.46
^{150}Nd	0.03	3.9	1.35
^{150}Nd	0.04	3.9	1.35
^{150}Nd	0.05	3.8	1.25
^{150}Nd	0.06	3.9	1.35
^{150}Nd	0.07	3.9	1.35
^{130}Te	0.01	2.1	1.27
^{130}Te	0.02	1.9	0.94
^{130}Te	0.03	2.2	1.46
^{130}Te	0.04	2.1	1.27
^{130}Te	0.05	1.9	0.94
^{130}Te	0.06	2.3	1.66
^{130}Te	0.07	1.8	0.80

388 method for the high Q -value isotope.

389 V. DISCUSSION

390 A. Comparison of effective neutrino mass obtained by 391 different isotopes

392 For $0\nu\beta\beta$ experiments, the effective neutrino mass $\langle m_{\beta\beta} \rangle$
393 is also of greater interest, which satisfying the following rela-
394 tionship [38]

$$395 T_{1/2}^{0\nu} = G_{0\nu} g_A^4 |M_{0\nu}|^2 \left| \frac{\langle m_{\beta\beta} \rangle}{m_e} \right|^2, \quad (14)$$

396 where g_A is the coupling constant, m_e is the electron mass,
397 and $G_{0\nu}$ and $M_{0\nu}$ are the phase space factor and nuclear ma-
398 trix element related to the isotope, respectively. For the phase
399 space factor $G_{0\nu}$, ^{150}Nd is around 4 times that of ^{130}Te [39],
400 while for the nuclear matrix element $M_{0\nu}$, there is a large
401 theoretical uncertainty [40–46].

402 As shown in Fig. 11, the 90% C.L. sensitivities of $\langle m_{\beta\beta} \rangle$
403 of ^{150}Nd are better than those of ^{130}Te in the same en-
404 ergy resolution, the method for sensitivity calculations and
405 the model for the calculation of the nuclear matrix element
406 (QRPA model and IBM model) [39]. As a result, for better
407 $\langle m_{\beta\beta} \rangle$ sensitivity, natural Nd is a better choice than natural
408 Te at the same loading mass fraction.

409 B. The sharp decline of sensitivity when fitting with Nd-150

410 The sensitivity of the fitting method with ^{150}Nd shows a
411 sharp decline at the energy resolution $6\%/\sqrt{E(\text{MeV})}$, as

412 shown in Fig. 10. This feature arises from the $2\nu\beta\beta$ back-
413 ground of ^{150}Nd . As energy resolution deteriorates, the $2\nu\beta\beta$
414 background starts to overlap more and more $0\nu\beta\beta$ signals,
415 leading to a significant drop in the performance of the fitting
416 method, as shown in Fig. 12(a).

417 Fig. 12(b) shows the background events in $[Q - \sigma, Q + \sigma]$,
418 where Q is the Q -value of ^{150}Nd and σ is the standard varia-
419 tion of the ^{150}Nd $0\nu\beta\beta$ signals. The background rate is indi-
420 cated to increase rapidly with the deterioration of the energy
421 resolution, providing evidence that $2\nu\beta\beta$ is an important fac-
422 tor that affects the sensitivity of ^{150}Nd .

423 The sharp decline of ^{150}Nd results in its sensitivity be-
424 ing lower than that of ^{130}Te at an energy resolution of
425 $7\%/\sqrt{E(\text{MeV})}$. One of the reasons is that ^{150}Nd has more
426 $2\nu\beta\beta$ background, and the other reason is that the natu-
427 ral abundance of ^{150}Nd (5.7%) is lower than that of ^{130}Te
428 (34.2%).

429 VI. CONCLUSION

430 In this research, we focus on the comparison of counting
431 and fitting method in $0\nu\beta\beta$ experiments. Based on simula-
432 tion of a 500m^3 spherical liquid scintillator detector at CJPL,
433 the $0\nu\beta\beta$ half-life sensitivities obtained from the counting
434 and fitting methods were compared with an energy resolution
435 of $1\%/\sqrt{E(\text{MeV})}$ to $7\%/\sqrt{E(\text{MeV})}$. We also performed
436 a fiducial volume cut for both methods and checked the ROI
437 selection for the counting method. Furthermore, ^{150}Nd and
438 ^{130}Te were chosen as representations of isotopes of high Q
439 and low Q values.

440 The results of this research indicate that the fitting method
441 obtains a higher sensitivity than the counting method for
442 the energy resolution of $1\%/\sqrt{E(\text{MeV})}$ to $7\%/\sqrt{E(\text{MeV})}$.
443 Furthermore, this research shows that given the equivalent en-

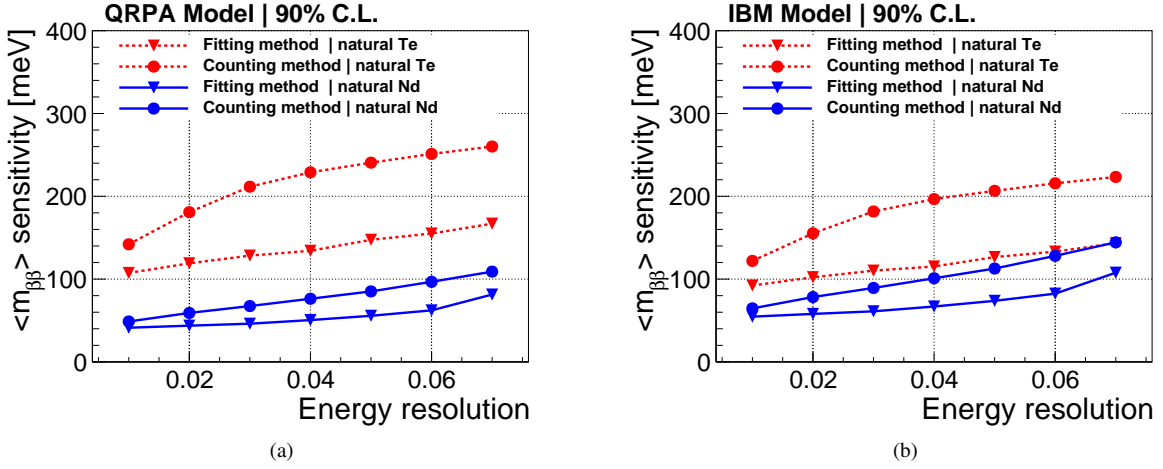


Fig. 11. The 90% C.L. sensitivities of effective neutrino mass vs. energy resolution. The red dashed lines are results derived with 1% natural Te-loaded and the blue solid lines are results derived with 1% natural Nd-loaded. The $G^{0\nu}$ and $M_{0\nu}$ are taken from QRPA model (a) and IBM model (b) data in Ref [39].

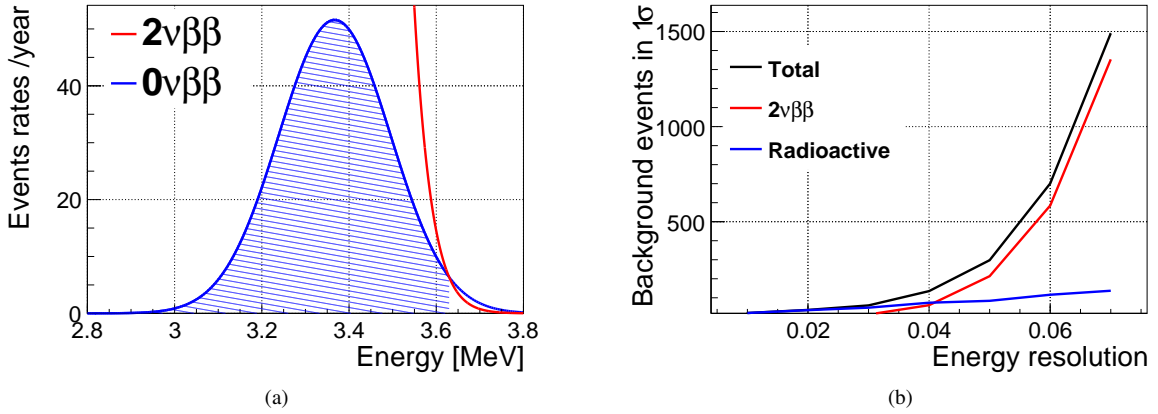


Fig. 12. (a) The ^{150}Nd $0\nu\beta\beta$ overlapped ratio drawn with an energy resolution of $7\%/\sqrt{E(\text{MeV})}$. The red line is the $2\nu\beta\beta$ background and the blue line is $0\nu\beta\beta$ signal. The dashed area is the overlapped $0\nu\beta\beta$ signals. The half-life of $0\nu\beta\beta$ is set at 5×10^{25} years, which is approximately the average sensitivity obtained in Section IV C. (b) The background events in one year for 1% natural Nd-loaded in the energy range $[Q - \sigma, Q + \sigma]$, where Q is the Q -value of $0\nu\beta\beta$ and σ is standard variation of $0\nu\beta\beta$ signals. The solar neutrino background is neglected, since they are much smaller than the other backgrounds.

444 ergy resolution, run time, and loading mass fraction, the ef-
 445 fective neutrino mass $\langle m_{\beta\beta} \rangle$ derived from natural Nd is lower
 446 than that derived from natural Te. This research could provide
 447 guidance for future experiments in selecting the appropriate
 448 method for sensitivity calculations and $0\nu\beta\beta$ isotopes.

449 We chose the energy resolution of $3\%/\sqrt{E(\text{MeV})}$ as a
 450 typical value of the liquid scintillator detector. Under this
 451 energy resolution and an exposure of 1.35 ton-year for ^{150}Nd
 452 and 1.46 ton-year for ^{130}Te , the better sensitivity comes from

453 the fitting method, as

$$^{150}\text{Nd} : 6.34 \times 10^{25} \text{ yr (90\% C.L.)}$$

$$^{130}\text{Te} : 4.50 \times 10^{25} \text{ yr (90\% C.L.)}$$

455 These $0\nu\beta\beta$ half-life correspond to the effective neu-
 456 trino mass $\langle m_{\beta\beta} \rangle$ 43-93 meV for ^{150}Nd and 76-150 meV for
 457 ^{130}Te .

458 [1] M.J. Dolinski, A.W.P. Poon, W. Rodejohann, Neutrino- 460 Nucl. Part. Sci. **69**, 219–251 (2019). [arXiv:1902.04097](https://arxiv.org/abs/1902.04097),
 459 less double-beta decay: Status and prospects. Ann. Rev.

461 doi:10.1146/annurev-nucl-101918-023407

462 [2] W. Rodejohann, Neutrino-less double beta decay and par-
463 ticle physics. *Int. J. Mod. Phys. E* **20**, 1833–1930 (2011).
464 arXiv:1106.1334, doi:10.1142/S0218301311020186

465 [3] Z. Zeng, Y.H. Mi, M. Zeng, et al., Characterization of a broad-
466 energy germanium detector for its use in cjpl. *Nucl. Sci. Tech.*
467 **28**, 7 (2017). doi:10.1007/s41365-016-0162-y

468 [4] W.H. Dai, et al., Search for neutrinoless double-beta de-
469 cay of ge76 with a natural broad energy germanium detec-
470 tor. *Phys. Rev. D* **106**, 032012 (2022). arXiv:2205.10718,
471 doi:10.1103/PhysRevD.106.032012

472 [5] I. Nutini, et al., Latest results from the cuore experiment. *J. Low Temp. Phys.* **209**, 927–935 (2022). doi:10.1007/s10909-022-02873-y

473 [6] E. Armengaud, et al., New limit for neutrinoless double-
474 beta decay of ^{100}mo from the cupid-mo experiment. *Phys. Rev. Lett.* **126**, 181802 (2021). arXiv:2011.13243,
475 doi:10.1103/PhysRevLett.126.181802

476 [7] W. Chen, L. Ma, J.H. Chen, et al., Gamma-, neutron-, and muon-induced environmental background simulations for
477 ^{100}mo -based bolometric double-beta decay experiment at jin-
478 ping underground laboratory. *Nucl. Sci. Tech.* **34**, 135 (2023). arXiv:2206.09288, doi:10.1007/s41365-023-01299-9

479 [8] M. Agostini, et al., Final results of gerda on the search for neu-
480 trinoless double- β decay. *Phys. Rev. Lett.* **125**, 252502 (2020). arXiv:2009.06079, doi:10.1103/PhysRevLett.125.252502

481 [9] X. Yan, et al., Searching for two-neutrino and neutrino-
482 less double beta decay of $\text{xe}134$ with the pandax-4t experi-
483 ment. *Phys. Rev. Lett.* **132**, 152502 (2024). arXiv:2312.15632,
484 doi:10.1103/PhysRevLett.132.152502

485 [10] W. Feldmeier, Search for neutrinoless double beta decay in
486 ^{136}xe with exo-200. Ph.D. thesis, Munich, Tech. U. (2015)

487 [11] A. Gando, et al., Search for majorana neutrinos near
488 the inverted mass hierarchy region with kamland-zen. *Phys. Rev. Lett.* **117**, 082503 (2016). [Addendum: *Phys. Rev. Lett.* **117**, 109903 (2016)]. arXiv:1605.02889,
489 doi:10.1103/PhysRevLett.117.082503

490 [12] S. Abe, et al., Search for the majorana nature of neu-
491 trinos in the inverted mass ordering region with kamland-
492 zen. *Phys. Rev. Lett.* **130**, 051801 (2023). arXiv:2203.02139,
493 doi:10.1103/PhysRevLett.130.051801

494 [13] X.G. Cao, et al., $\text{N}\nu\text{dex-100}$ conceptual design re-
495 port. *Nucl. Sci. Tech.* **35**, 3 (2024). arXiv:2304.08362,
496 doi:10.1007/s41365-023-01360-7

497 [14] C.F. Yang, Y.B. Huang, J.L. Xu, et al., Reconstruction of a
498 muon bundle in the juno central detector. *Nucl. Sci. Tech.* **33**,
499 59 (2022). arXiv:2201.11321, doi:10.1007/s41365-022-01049-
500 3

501 [15] Y.Y. Ding, M.C. Liu, L.J. Wen, et al., A novel approach
502 in synthesizing te-diol compounds for tellurium-loaded liq-
503 uid scintillator. *Nucl. Instrum. Meth. A* **1049**, 168111 (2023).
504 doi:10.1016/j.nima.2023.168111

505 [16] V. Albanese, et al., The sno+ experiment. *JINST* **16**,
506 P08059 (2021). arXiv:2104.11687, doi:10.1088/1748-
507 0221/16/08/P08059

508 [17] I.R. Barabanov, et al., Searches for neutrinoless double-beta
509 decay of the isotope ^{150}nd by means of a liquid organic
510 scintillator detector. *Phys. Atom. Nucl.* **82**, 89–97 (2019).
511 doi:10.1134/S1063778819020029

512 [18] W. Luo, Q. Liu, Y. Zheng, et al., Reconstruction algo-
513 rithm for a novel cherenkov scintillation detector. *JINST*
514 **18**, P02004 (2023). arXiv:2209.13772, doi:10.1088/1748-
515 0221/18/02/P02004

516 [19] Z. Guo, et al., Muon flux measurement at china jinping
517 underground laboratory. *Chin. Phys. C* **45**, 025001 (2021).
518 arXiv:2007.15925, doi:10.1088/1674-1137/abccae

519 [20] W.H. Zeng, H. Ma, M. Zeng, et al., Evaluation of cosmogenic
520 activation of copper and germanium during production in jin-
521 ping underground laboratory. *Nucl. Sci. Tech.* **31**, 50 (2020).
522 doi:10.1007/s41365-020-00760-3

523 [21] K. Zuber, *Neutrino Physics*, (Taylor & Francis, Boca Raton,
524 2020). doi:10.1201/9781315195612

525 [22] H. Primakoff, S.P. Rosen, Double beta decay. *Rept. Prog. Phys.*
526 **22**, 121–166 (1959). doi:10.1088/0034-4885/22/1/305

527 [23] A. Serenelli, Alive and well: a short review about standard so-
528 lar models. *Eur. Phys. J. A* **52**, 78 (2016). arXiv:1601.07179,
529 doi:10.1140/epja/i2016-16078-1

530 [24] S.M. Bilenky, Neutrino masses, mixing and oscillations. *Prog. Part. Nucl. Phys.* **57**, 61–67 (2006). arXiv:hep-ph/0510175,
531 doi:10.1016/j.ppnp.2005.10.001

532 [25] L. Baudis, A. Ferella, A. Kish, et al., Neutrino physics with
533 multi-ton scale liquid xenon detectors. *JCAP* **01**, 044 (2014).
534 arXiv:1309.7024, doi:10.1088/1475-7516/2014/01/044

535 [26] H. Ejiri, S.R. Elliott, Solar neutrino interactions with
536 the double beta decay nuclei of ^{82}se , ^{100}mo and
537 ^{150}nd . *Phys. Rev. C* **95**, 055501 (2017). arXiv:1703.06915,
538 doi:10.1103/PhysRevC.95.055501

539 [27] H. Ejiri, S.R. Elliott, Charged current neutrino cross sec-
540 tion for solar neutrinos, and background to $\beta\beta(0\nu)$ exper-
541 iments. *Phys. Rev. C* **89**, 055501 (2014). arXiv:1309.7957,
542 doi:10.1103/PhysRevC.89.055501

543 [28] E.J. Konopinski, Beta-Decay. *Rev. Mod. Phys.* **15**, 209–245
544 (1943). doi:10.1103/RevModPhys.15.209

545 [29] C. Arpesella, et al., Measurements of extremely low radioac-
546 tivity levels in borexino. *Astropart. Phys.* **18**, 1–25 (2002).
547 arXiv:hep-ex/0109031, doi:10.1016/S0927-6505(01)00179-7

548 [30] SNO collaboration, Sno technical reports. (2022)
549 https://sno.phy.queensu.ca/str/rad.html

550 [31] G. Hussain, Z. Zeng, C. Yao, et al., Assay of low-
551 background stainless steel by smelting for the neutrino exper-
552 iment at jinping. *Nucl. Instrum. Meth. A* **881**, 65–71 (2018).
553 arXiv:1706.04506, doi:10.1016/j.nima.2017.11.006

554 [32] S. Dell’Oro, S. Marcocci, M. Viel, et al., Neutrino-
555 less double beta decay: 2015 review. *Adv. High Energy Phys.* **2016**, 2162659 (2016). arXiv:1601.07512,
556 doi:10.1155/2016/2162659

557 [33] X. Ji, W. Gu, X. Qian, et al., Combined neyman–pearson chi-
558 square: An improved approximation to the poisson-likelihood
559 chi-square. *Nucl. Instrum. Meth. A* **961**, 163677 (2020).
560 arXiv:1903.07185, doi:10.1016/j.nima.2020.163677

561 [34] R. Brun, F. Rademakers, Root: An object oriented data anal-
562 ysis framework. *Nucl. Instrum. Meth. A* **389**, 81–86 (1997).
563 doi:10.1016/S0168-9002(97)00048-X

564 [35] G.J. Feldman, R.D. Cousins, A unified approach to
565 the classical statistical analysis of small signals. *Phys. Rev. D* **57**,
566 3873–3889 (1998). arXiv:physics/9711021,
567 doi:10.1103/PhysRevD.57.3873

568 [36] T.M. Karbach, Feldman-cousins confidence levels - toy mc
569 method. arXiv preprint arXiv:1109.0714. arXiv:1109.0714

570 [37] M.A. Acero, et al., The profiled feldman-cousins technique for
571 confidence interval construction in the presence of nuisance pa-
572 rameters. arXiv preprint arXiv:2207.14353. arXiv:2207.14353

573 [38] F.T. Avignone, III, S.R. Elliott, J. Engel, Double beta
574 decay, majorana neutrinos, and neutrino mass. *Rev. Mod. Phys.* **80**,
575 481–516 (2008). arXiv:0708.1033,
576 doi:10.1103/RevModPhys.80.481

587 [39] R.G.H. Robertson, Empirical survey of neutrinoless double 602
 588 beta decay matrix elements. *Mod. Phys. Lett. A* **28**, 1350021 603
 589 (2013). [arXiv:1301.1323](https://arxiv.org/abs/1301.1323), doi:10.1142/S0217732313500211 604

590 [40] J. Menendez, A. Poves, E. Caurier, et al., Disassembling 605
 591 the nuclear matrix elements of the neutrinoless beta beta de- 606
 592 cay. *Nucl. Phys. A* **818**, 139–151 (2009). [arXiv:0801.3760](https://arxiv.org/abs/0801.3760), 607
 593 doi:10.1016/j.nuclphysa.2008.12.005 608

594 [41] J. Barea, F. Iachello, Neutrinoless double-beta decay in the mi- 609
 595 croscopic interacting boson model. *Phys. Rev. C* **79**, 044301 610
 596 (2009). doi:10.1103/PhysRevC.79.044301 611

597 [42] T.R. Rodriguez, G. Martinez-Pinedo, Energy density func- 612
 598 tional study of nuclear matrix elements for neutrinoless $\beta\beta$ 613
 599 decay. *Phys. Rev. Lett.* **105**, 252503 (2010). [arXiv:1008.5260](https://arxiv.org/abs/1008.5260), 614
 600 doi:10.1103/PhysRevLett.105.252503 615

601 [43] P.K. Rath, R. Chandra, K. Chaturvedi, et al., Uncertainties 616
 in nuclear transition matrix elements for neutrinoless $\beta\beta$ de-
 cay within the phfb model. *Phys. Rev. C* **82**, 064310 (2010).
[arXiv:1104.3965](https://arxiv.org/abs/1104.3965), doi:10.1103/PhysRevC.82.064310

605 [44] F. Simkovic, A. Faessler, H. Muther, et al., The 0 nu bb-de-
 606 cay nuclear matrix elements with self-consistent short-range cor-
 607 relations. *Phys. Rev. C* **79**, 055501 (2009). [arXiv:0902.0331](https://arxiv.org/abs/0902.0331),
 608 doi:10.1103/PhysRevC.79.055501

609 [45] D.L. Fang, A. Faessler, V. Rodin, et al., Neutrinoless 610
 611 double-beta decay of ^{150}Nd accounting for deformation. *Phys. Rev. C* **82**, 051301 (2010). [arXiv:1009.5579](https://arxiv.org/abs/1009.5579),
 612 doi:10.1103/PhysRevC.82.051301

613 [46] O. Civitarese, J. Suhonen, Nuclear matrix elements for dou- 614
 615 ble beta decay in the qrpa approach: A critical review. *J. Phys. Conf. Ser.* **173**, 012012 (2009). doi:10.1088/1742-
 616 6596/173/1/012012